Article

VIIRS Nightfire: Satellite Pyrometry at Night

Christopher D. Elvidge [1],*, Mikhail Zhizhin [2], Feng-Chi Hsu [2] and Kimberly E. Baugh [2]

[1] Earth Observation Group, NOAA National Geophysical Data Center, Boulder, CO 80305, USA
[2] Cooperative Institute for Research in Environmental Science, University of Colorado, Boulder, CO 80309, USA; E-Mails: mikhail.zhizhin@noaa.gov (M.Z.); feng-chi.hsu@noaa.gov (F.H.); kim.baugh@noaa.gov (K.B.)

* Author to whom correspondence should be addressed; E-Mail: chris.elvidge@noaa.gov; Tel.: +1-303-497-6121; Fax: +1-303-497-6513.

Abstract: The Nightfire algorithm detects and characterizes sub-pixel hot sources using multispectral data collected globally, each night, by the Suomi National Polar Partnership (NPP) Visible Infrared Imaging Radiometer Suite (VIIRS). The spectral bands utilized span visible, near-infrared (NIR), short-wave infrared (SWIR), and mid-wave infrared (MWIR). The primary detection band is in the SWIR, centered at 1.6 μm. Without solar input, the SWIR spectral band records sensor noise, punctuated by high radiant emissions associated with gas flares, biomass burning, volcanoes, and industrial sites such as steel mills. Planck curve fitting of the hot source radiances yields temperature (K) and emission scaling factor (ESF). Additional calculations are done to estimate source size (m^2), radiant heat intensity (W/m^2), and radiant heat (MW). Use of the sensor noise limited M7, M8, and M10 spectral bands at night reduce scene background effects, which are widely reported for fire algorithms based on MWIR and long-wave infrared. High atmospheric transmissivity in the M10 spectral band reduces atmospheric effects on temperature and radiant heat retrievals. Nightfire retrieved temperature estimates for sub-pixel hot sources ranging from 600 to 6,000 K. An intercomparison study of biomass burning in Sumatra from June 2013 found Nightfire radiant heat (MW) to be highly correlated to Moderate Resolution Imaging Spectrometer (MODIS) Fire Radiative Power (MW).

Keywords: SNPP; VIIRS; fire detection; gas flaring; biomass burning; fossil fuel carbon emissions

1. Introduction

A pyrometer is a non-contacting instrument that measures radiation emitted by hot objects. Satellite pyrometry is a favored approach for the global detection and characterization of combustion sources. Variables of interest that can potentially be derived from satellite based pyrometric data include temperature, source size, heat release, combustion efficiency, fuel consumption rate, and composition of combustion sources. Satellite based pyrometry has a proven track record of successful detection of combustion sources. Fire characterization is limited by the sensors, how the sensors are operated, and how the data are processed.

Thermal infrared data collected by Earth observing satellites have been used for pyrometry since the 1980s [1,2]. Satellite data collected by NOAA's Geostationary Operational Environmental Satellites (GOES), Advanced Very High Resolution Radiometer (AVHRR), NASA's Moderate Resolution Imaging Spectrometer (MODIS), and the NASA/NOAA Visible Infrared Imaging Radiometer Suite (VIIRS) are currently used for both regional and global detection of hot spots, with a focus on the detection of biomass burning [3–5] These data are useful to government agencies engaged in managing fires and by-products such as carbon emissions, smoke, and haze.

The fundamental basis of pyrometry is Planck's Law, which defines the emission spectra of blackbodies based on their absolute temperature. The general equation of Planck's Law is shown below:

$$R = \frac{2hc^2}{\lambda^5} \frac{1}{\exp(hc/(\lambda k_B T)) - 1} \tag{1}$$

where R denotes spectral radiance, λ is the wavelength, T is the absolute temperature of the material (K), k_B is the Boltzmann constant, h is the Planck constant, and c is the speed of light. Planck's Law serves as the foundation for two additional laws that are important to pyrometric calculations.

Wien's Displacement Law states that as the temperature of an object increases the wavelength of peak radiant emission shifts to shorter wavelengths.

$$\lambda_m = A/T \tag{2}$$

where λ_m is the wavelength of maximum spectral radiant emittance, A is Wien's displacement constant, and T is the absolute temperature of the black body (K). With this law, it is possible to calculate the temperature of a sub-pixel source if the wavelength of peak radiant emission can be determined.

With an estimate of temperature, it is possible to calculate total radiant output using the Stefan-Boltzmann's Law.
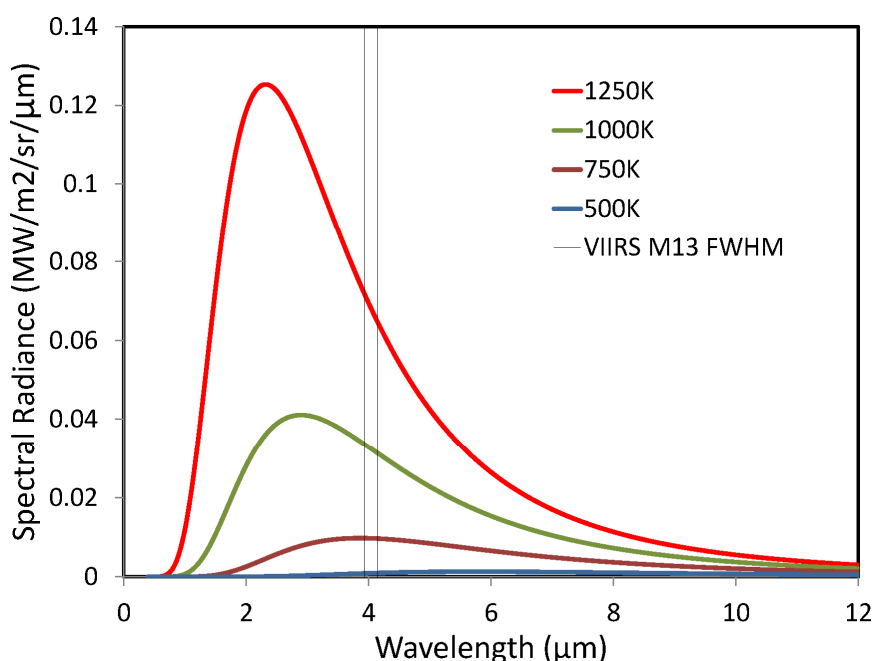
$$I = \varepsilon \sigma T^4 \tag{3}$$

where I is the total radiant output from the surface of a material (W/m^2), σ is Stefan-Boltzmann Constant, T is the absolute temperature of the emitting material (K), and ε is the emissivity of a material.

There are two main branches to pyrometry: full field-of-view and sub-pixel. In full field-of-view pyrometry, the object being measured fills the entire field-of-view of the sensor. The temperature of the object can estimated based on the emitted radiance in a single spectral channel (Figure 1). This technique relies on the progressive increase in emitted radiance as the temperature of an object increases, as expression of the Stefan-Boltzmann's Law. There is no need to locate the wavelength of peak radiant emission, since the Planck curves do not cross or intersect. Full field of view pyrometry

can be achieved with ground-based pyrometers and with high spatial resolution remote sensing data. There are three considerations in the selection of a suitable spectral band for full field of view pyrometry: (1) The spectral band should cover a bandpass where there are significant changes in emitted radiance for the temperature range of interest, (2) the bandpass should be located in a relatively clear atmospheric window, and (3) the bandpass should be largely free of solar contamination, to work well, both day and night. For day and night full field of view pyrometry, the spectral range of choice is in the 3–5 μm atmospheric window, which has low solar irradiance and measureable radiant emissions spanning a wide range of temperatures.

> **Figure 1.** When the hot object fills the entire field of view, the temperature of the object can be estimated based on the radiance observed in a single spectral band that is clear of radiance from external sources. Knowledge of the emissivity of the object and an atmospheric correction can improve the accuracy of the temperature estimate.

In most cases, satellite detections of "hot pixels" involve sub-pixel sources that are substantially smaller than the pixel footprint. In this case the emitted radiance has both a background and a hot source component. The longwave background component is the radiance emitted by the Earth surface and atmosphere (e.g., clouds), with a Planck curve centered in the 8–12 μm atmospheric window. The shortwave scene background is reflected sunlight. The presence of a hot source is indicated by anomalously high radiances or brightness temperatures at shorter wavelengths, which cannot be attributed to reflected sunlight.

A bi-spectral sub-pixel pyrometry technique was pioneered for satellite remote sensing data by Dozier [1], who worked with nighttime data from the mid-wave infrared (MWIR) and long-wave infrared (LWIR) AVHRR data. It was observed that pixels containing hot sources had higher brightness temperatures in the 3.7 μm (MWIR) channel when compared to the local background. Some of the MWIR hotspots also had elevated brightness temperatures in the 11 μm (LWIR) channel. In the classic Dozier method, the temperature and size of a sub-pixel hot source can be calculated if the

temperature of the background can be reasonably determined and if there is a detectable hot source signal in both the MWIR and LWIR channels.

While the technique to calculate the temperature and size of sub-pixel hot sources was demonstrated, the approach has not been operationally implemented for data from AVHRR or its follow on systems (e.g., NASA's Moderate Resolution Imaging Spectrometer (MODIS) and the NASA/NOAA Visible Infrared Imaging Radiometer Suite (VIIRS)) due to several complications. While large numbers of hot pixels can be detected with MWIR channel data, relatively few of those pixels also have anomalously high brightness temperature in the LWIR region, which eliminates the Dozier calculation as an option. Dozier method error sources include differences in pointing and point-spread function between the MWIR and LWIR pixels, errors in background temperature estimates, atmospheric correction errors, temperature variations in extended hot sources, and saturation in the MWIR spectral band [2–5]. Giglio and Kendall [2] examined these issues and concluded: "Limitations in current moderate resolution sensors make Dozier's technique for fire property retrieval operationally useful for only stable, uniform high temperature sources over very uniform backgrounds such as gas flares on offshore oil platforms."

Following Dozier's lead, the standard fire product from MODIS is processed from a pair of spectral bands (MWIR and LWIR) [6,7]. The product indicates the pixels containing hot sources, but provides no estimate of the temperature or source size. In lieu of Planck curve fitting, the MODIS active fire product provides an estimate of Fire Radiative Power using Kaufman's 1998 formula [8], empirically derived from field observations of fuel consumption rates for vegetation fires ranging from smoldering (600 K ± 100 K) to flaming (1,000 K ± 200 K). At present, the VIIRS active fire product simply indicates the pixels with hot source detection.

The inquiry that led to Nightfire arose from a project to improve the quality of natural gas flaring estimates from satellite data sources. Initially, these estimates were produced from DMSP (Defense Meteorological Satellite Program) nighttime lights data, collected in a single panchromatic spectral band [9]. The DMSP low light imaging data could be termed semi-quantitative, since there is no in-flight calibration and there is typically saturation in city centers and gas flares. Several years ago the authors explored MODIS data and found that large gas flares had relatively weak signals in the MWIR MODIS channel used in fire detection. What we did not realize is that flares burn at such a high temperature that the peak radiant emissions are at substantially shorter wavelengths. The MWIR is literally on the trailing edge of the gas flare emission spectrum. Thus, even largest gas flares will have modest radiant emissions in the MWIR.

When VIIRS data became available, the authors decided to examine images from each of the spectral bands collected by VIIRS to discover which ones may be useful for detecting and characterizing gas flares. The daytime collections looked very similar to MODIS. At night, VIIRS collects data in nine spectral bands (Table 1 and Figure 2). In reviewing nighttime images collected over well-known gas flaring regions, it was discovered that gas flares have a strong signal in data collected by the 1.6 μm channel (M10) at night. The flare features are generally too weak to be detected in daytime M10 data due to solar reflectance. At night the vast majority of the M10 pixels are recording system noise, which is dominated by dark current, the signal a radiometer records when light is blocked from entry into the aperture. Pixels with hot sources stand out clearly against the system noise in nighttime M10 data. These 1.6 μm nighttime phenomena have been previously reported with

ATSR data [10,11]. The M7 and M8 data collected at night by VIIRS show a similar capability to detect pixels containing hot sources. The low light imaging day-night band (DNB) detects both electric lighting and combustion sources. Some of the larger flares can be identified in the mid-wave infrared images (M12 and M13), however algorithmic detection here is complicated by scene feature content, which is dominated by temperature differences between different surface types and clouds. Hot pixel detections decline as wavelength increases, with very little expression of hot pixel radiance in the LWIR channels (M14, M15, and M16).

Table 1. Characteristics of the Nine Visible Infrared Imaging Radiometer Suite (VIIRS) Spectral Bands Collecting Data at Night [12]

Band Designation	Spectral Range	Bandpass (μm)	Band Center (μm)	Lmin (W/(m²·μm·sr)) Requirement	Lmax (W/(m²·μm·sr)) Requirement
DNB	Panchromatic	0.5–0.9	0.7	$3.0E^{-5}$ W/(m²·sr)	200 W/(m²·sr)
M7	Near infrared	0.843–0.881	0.862	3.4	349
M8	Near infrared	1.225–1.252	1.2385	3.5	164.9
M10	Short-wave IR	1.571–1.631	1.601	1.1	71.2
M12	Mid-wave IR	3.598–3.791	3.6945	0.0078	2.84
M13	Mid-wave IR	3.987–4.145	4.066	0.00216	406
M14	Long-wave IR	8.407–8.748	8.5775	0.373	19.5
M15	Long-wave IR	10.234–11.248	10.741	0.729	17.1
M16	Long-wave IR	11.405–12.322	11.865	0.876	14.5

Based on these findings, the authors decided to develop a new multispectral pyrometric system for nighttime VIIRS data and to base the initial detection of hot pixels on the M10 spectral channel. This paper outlines the algorithm and data from the resulting system, which we refer to as Nightfire.

Figure 2. Sample images of Southern Iraq from the nine VIIRS spectral bands which collect data at night. The area has a large number of persistent gas flares.
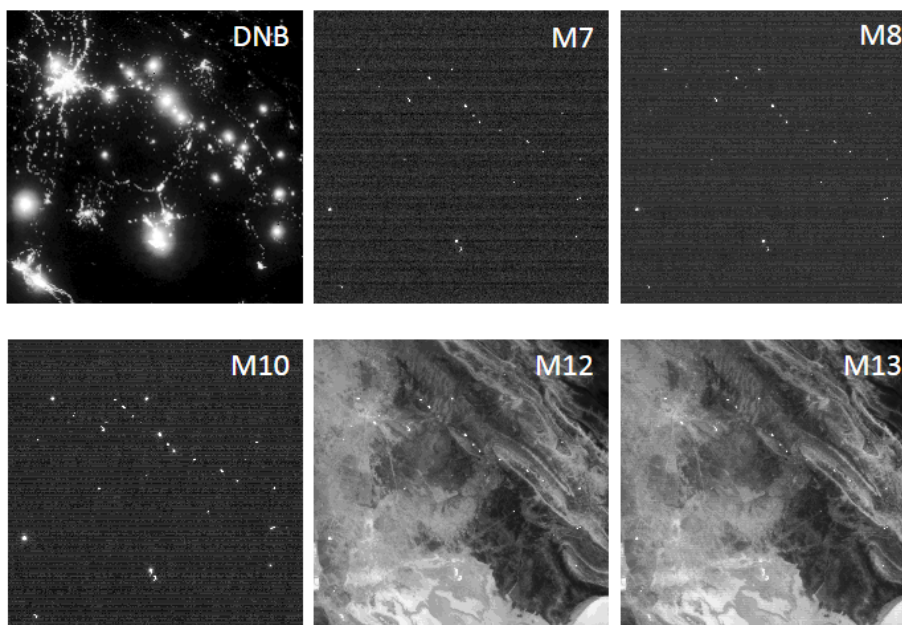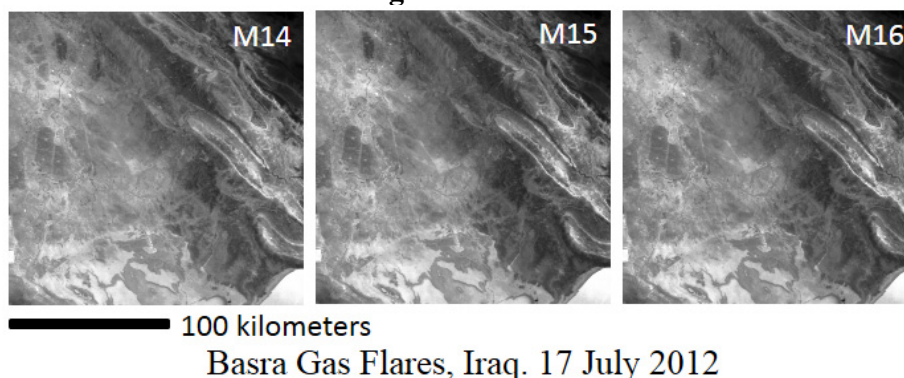
Figure 2. *Cont.*

100 kilometers

Basra Gas Flares, Iraq. 17 July 2012

2. Methods

The hot source detection component of Nightfire runs on VIIRS SDR (Sensor Data Records) files. Cloud conditions are rated using the VIIRS cloud mask and cloud optical thickness products. The MODTRAN 5 [13] atmospheric correction is parameterized with atmospheric temperature and water vapor profiles produced from data collected by the Advanced Technology Microwave Sounder (ATMS) and Cross-track Infrared Sounder (CrIS) instruments [14], collected simultaneously to the VIIRS data. The global version of Nightfire currently runs on a 24 hour delay on data delivered to National Geophysical Data Center (NGDC) for archive.
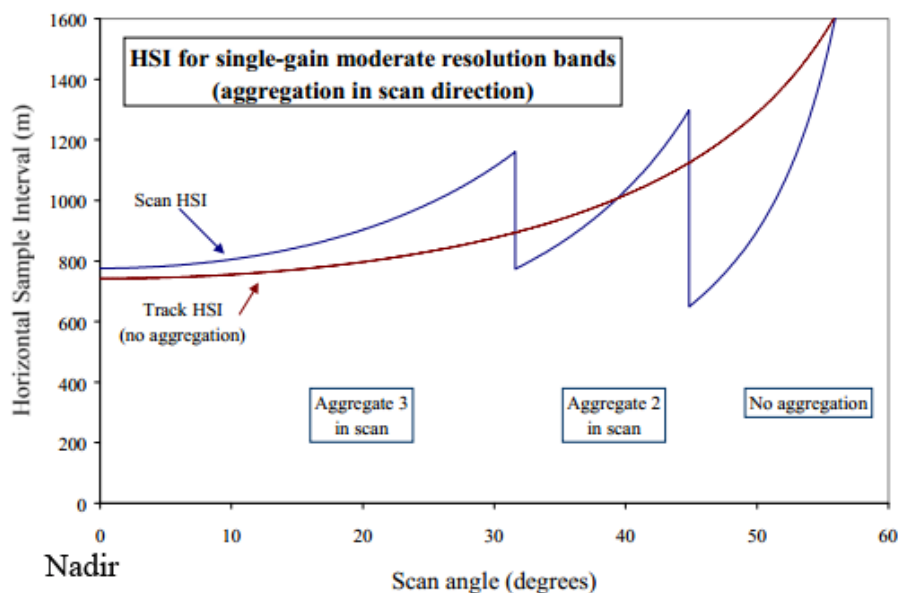
2.1. Detection of Hot Pixels in the M10 Band

At night the M10 spectral band records the noise of the instrument, except for the few pixels which contain an infrared emitter, such as a gas flare, biomass burning, or hot lava. The set of candidate pixels containing sub-pixel hot sources are identified based on anomalously high values in the M10 spectral band centered at 1.6 μm [15]. Data with solar contamination are excluded by thresholding out pixels that have solar zenith angles less than 95 degrees. The outline of the useable pixel set is recorded for use in temporal compositing. The M10 hot pixel detection analysis is performed on the unsigned integers recorded in the SDR files. Each M10 SDR file has a scale and offset for converting the unsigned integers to radiances.

The VIIRS constrains the expansion of the M-band pixel footprints from nadir to the edge of scan by systematically varying the number of pixels aggregated on-board [12]. In the region ±31.72 degrees out from nadir, three pixels are aggregated (Figure 3). The instrument then switches to aggregate two pixels out to ±44.86 degrees. In the final segment of the scan (out to ±56.28 degrees) no aggregation is used and the instrument records signal from single pixels.

While successfully controlling the footprint size, this aggregation scheme alters the signal-to-noise ratios in the aggregation zones. To make Nightfire as sensitive as possible, three sets of means and standard deviations are calculated on each SDR file, pooling the pixels from the three pixel aggregation zones. Obvious hot pixels are excluded from the background pixel set by screening out digital values over 100. Both the mean and standard deviation become progressively higher as the number of pixels aggregated shifts from three, to two, and one (Figure 4). Candidate hot pixels are identified as those with digital numbers exceeding the mean plus four standard deviations. Details of the M10 hot pixels are recorded in a comma-separated value (CSV) file, including the unsigned

integer, radiance, source file name, line and sample numbers, latitudes and longitudes, quality flags, and other metadata.

> **Figure 3.** Horizontal sample interval chart shows how the growth of VIIRS M-band ground field of view from nadir to edge of scan is constrained by switching the number of pixels that are aggregated [12]. In aggregation zone 1, from nadir to 31.72 degrees, the signal from three pixels are averaged. In aggregation zone two, the signal from two pixels are averaged. In aggregation zone three, signal from a single pixel is recorded.
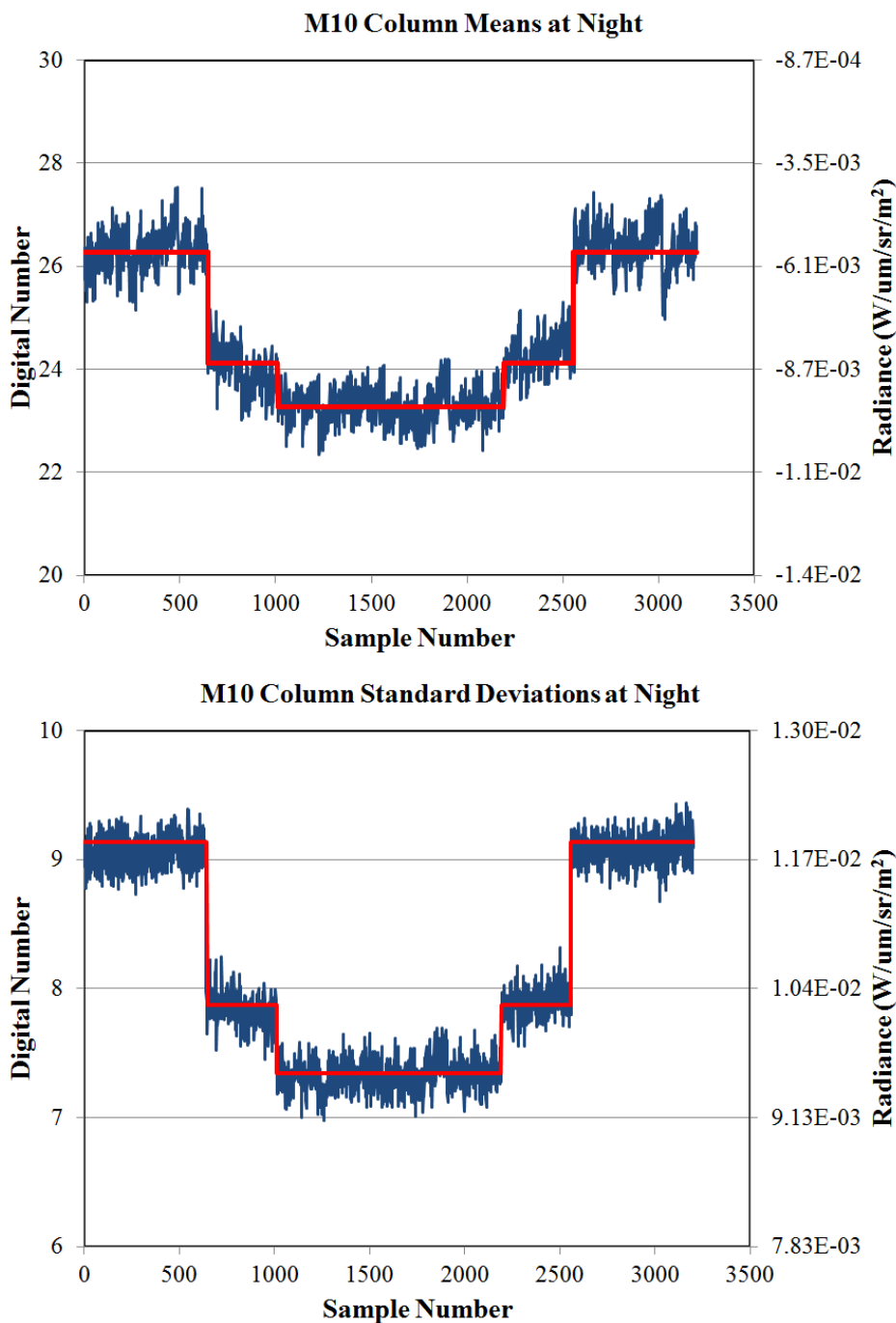

While all the M10 hot pixels are recorded in the CSV, currently only the pixels containing M10 local maxima are recorded in the Zipped KML (Keyhole Markup Language). The M10 local maxima are identified as pixels where the immediate neighbors have lower radiances. The local maxima are filtered to eliminate bowtie duplicates.

2.2. Processing of Other Spectral Bands

The line and sample numbers for the M10 hot pixels are used as guides to locate the corresponding pixels in the other seven M bands (M7–8, M12–16) for entry of the radiance values in the CSV. M7 and M13 are dual gain bands, with radiances recorded in the SDR. The SDR values in the other M bands are unsigned integers, with scale and offset recorded in the HDF5. For M8 and M12–16 the radiances are calculated from the unsigned integers prior to recording in the CSV.

Following this, the SDR data in M7–8 and M12–13 are analyzed to determine if the M10 hot pixels are also hot in the other spectral bands. The M7 and M8 are NIR bands, and, like the M10 band, the nighttime images contain instrument noise background with high values in pixels containing hot sources. Therefore, the same procedure to determine M10 hot pixel thresholds outlined in Section 2.1 is applied to M7 and M8. The M7 and M8 hot pixel detection thresholds are recorded in the CSV. Detection flags are set in the CSV to indicate the M7 and M8 hot pixels.

Figure 4. Charts show variability of column means and standard deviations for an M10 image collected over ocean with no combustion sources present the night of 5 March 2013. Note that the three detector aggregation zones show up in both the mean and standard deviation, which are lowest in zone 1 and step up incrementally in zone 2 and zone 3. The detection threshold analysis is performed on the unsigned integers provided in the SDR. These can be converted to radiances by applying a scale and offset. A slight error is indicated in the offset term, resulting in negative radiance values.

The M12 and M13 are MWIR bands, so the analysis is complicated by the presence of earth surface and cloud features. Thresholds for the M12 and M13 detection of hot pixels are calculated using a 10 by 10 window established for each M10 hot pixel. The M10 hot pixels are excluded and the remaining

pixels are used to calculate a mean plus standard deviation. If the number of background pixels found is less than 50, then the window is expanded to 100 by 100. Hot pixel detection thresholds are calculated as the background mean plus three standard deviations. All the hot pixel thresholds, radiances, SDR quality flags, and for M12 and M13 the average background radiance values, are also recorded in the CSV. Detection flags are set in the CSV to indicate the M12 and M13 hot pixels.

The DNB images have a different pixel width than the M-band images, so the M-band line and sample values cannot be used directly to extract the DNB radiances. Instead, the algorithm uses line and scan angle to get an approximate spatial match. Currently, the DNB values are only extracted for the M10 hot pixels that are also local maxima. For each M10 local maximum, a corresponding DNB local maxima is sought in the same line where the scan angles match. If a corresponding DNB local max is found, the radiance is recorded along with DNB quality flag, latitude, longitude, line, and sample values are also recorded.

2.3. Noise Filtering

The M10 nighttime data is subject to noise spikes due to high energy particle impacts on detectors in the South Atlantic Anomaly and in auroral zones. Most of this noise can be filtered by excluding M10 hot pixel detections that cannot be confirmed by hot pixel detections in at least one additional spectral band [15]. A detection flag is set to indicate the M10 pixels where the hot pixel is confirmed.

2.4. Atmospheric Correction

Nightfire can be run with or without an atmospheric correction. Coefficients for correcting losses in radiance due to atmospheric absorption and scatter are derived for each spectral band using MODTRAN 5 [13] parameterized with atmospheric temperature and water vapor profiles processed from the CrIS and ATMS sensors (CrIMSS data) [14].

2.5. Planck Curve Fitting

Planck curve fitting is applied using radiances from spectral bands that are above the detection thresholds using the Simplex Optimization Method [16]. For M7, M8, and M10, the observed radiances are used directly. For M12 and M13, the local background average, discussed in Section 2.2, is subtracted from the observed radiance. The sub-pixel hot sources appear as a graybodies, due to the fact that they only occupy a small portion of the pixel footprint on the ground. Therefore, we define the emissivity term in the Planck function as an *emission scaling factor* (ESF) and subsequently use ESF to estimate the source size.

The Planck curve fitting is done based on two variables: temperature and ESF. The initial temperature of the fitting procedure is 1,000 degrees K and an ESF of 1.0. The fitting typically converges on a solution within twenty iterations. The output of the fitting is an estimate of the temperature and ESF of the hot source present in the pixel, which are recorded in the CSV.

The Planck curve fitting results in unrealistically low temperatures for two categories of hot pixels. The most widely occurring type is for pixels with a M10 detection that are confirmed by a DNB detection, but unsupported by hot pixel detection in any of the other four spectral bands. These are the weakest detections coming from Nightfire. The Planck curve fitting gives unrealistic results because

the long wavelength side of the fitting (>1.6 μm) is unconstrained, resulting in an unreasonably low temperature. Currently, the temperature for two band detection pixels with DNB and M10 are set to 1,810 K, the temperature of an object with peak radiance in M10. The other category are pixels with large low temperature hot sources, where the combination of low M10 radiance and high radiances in M12 and M13 occasionally result in Planck curve fits that fail to pass through or close to the M10 radiance. This pixel category is discussed in more detail in Section 3.3.

2.6. Calculation of Source Area

Several additional calculations are made using temperature, ESF, and the M band pixel footprint size on the ground. The M band pixel footprint size (A) is the product of VIIRS along scan (ΔS) and along track pixel size (ΔT). ΔT and ΔS are derived from following equations:

$$\Delta S = R_e * Ss \left(\frac{\cos \theta}{\sqrt{((R_e/r)^2 - sin^2\theta)}} - 1 \right) * \frac{1}{x} \tag{4}$$

$$\Delta T = r * St \left(cos\theta - \sqrt{((R_e/r)^2 - sin^2\theta)} \right) \tag{5}$$

where Re = 6,378.137 km (radius of the Earth), H = 833 km (satellite nominal altitude), r = Re + H. Ss = px_x / H, St = px_y / H, where px_x = 0.776 km (pixel size along scan), px_t = 0.742 km (pixel size along track). To address the three pixel aggregation zones, the multiplier (x) is designated as follow:

$$x = \begin{cases} 1, if\ \theta \le 31.72° \\ 1.5, if\ 31.72° < \theta \le 44.86° \\ 3, if\ 44.86° < \theta \end{cases} \tag{6}$$

The source size (a) can be then derived in square meters by multiplying ESF by the estimated size of the sub-pixel hot M band pixel footprint from the following equation:

$$a = ESF * A = ESF * \Delta S * \Delta T \tag{7}$$

2.7. Calculation of Radiant Heat

The radiant heat intensity (I, in W/m^2) is calculated using Stefan-Boltzmann's Law with temperature (T) and ESF as inputs. Radiant heat (Q, in MW) is calculated by multiplying radiant heat intensity by the square meters of the pixel footprint as shown in the following equation:
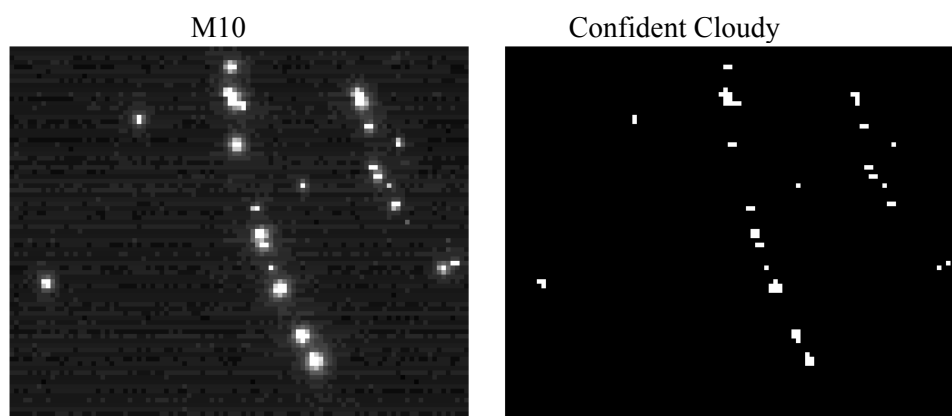
$$Q = I * A \tag{8}$$

For gas flares, an estimate is made of the quantity of methane combustion (m^3/s) required to produce the observed radiant heat [18]. This is termed "methane equivalents" since there are typically minor quantities of other hydrocarbons present. The methane equivalents are used to calculate carbon dioxide emission rates (g/s).

2.8. Treatment of Clouds

Clouds obscure combustion sources by absorbing radiant emissions. The obscuration can range from partial to total. Nightfire reports all hotspot detections and records the cloud conditions reported in the VIIRS cloud mask and cloud optical thickness products. With each VIIRS data aggregate there is typically an associated cloud mask and very often a cloud optical thickness product. The cloud mask has four values: 0 = confidently clear, 1 = probably clear, 2 = probably cloudy, and 3 = confidently cloudy [19]. The smallest of these classes in terms of spatial extent is 2 (probably cloudy) which rings the outer margins of almost every identified cloud features.

In examining the cloud mask, it was found that gas flares are frequently misidentified as having cloud cover (Figure 5). These are isolated patches marked as "probably cloudy" or "confidently cloudy". This may be a type of spectral confusion. A cloud-clearing algorithm is run to reset the cloud mask values for isolated clouds associated with M10 hot pixels.

Figure 5. Gas flares often have isolated patches of cloud in the VIIRS cloud mask.

Gas Flares Misidentified as Cloud

Only pixels deemed to be confidently cloudy have cloud optical thickness values. Some clouds are optically thin, with minimal impact on the radiances from hot sources. We identified pixels with optically thin clouds using an upper cloud optical thickness threshold of 0.01, corresponding to an atmospheric transmissivity value of 99%.
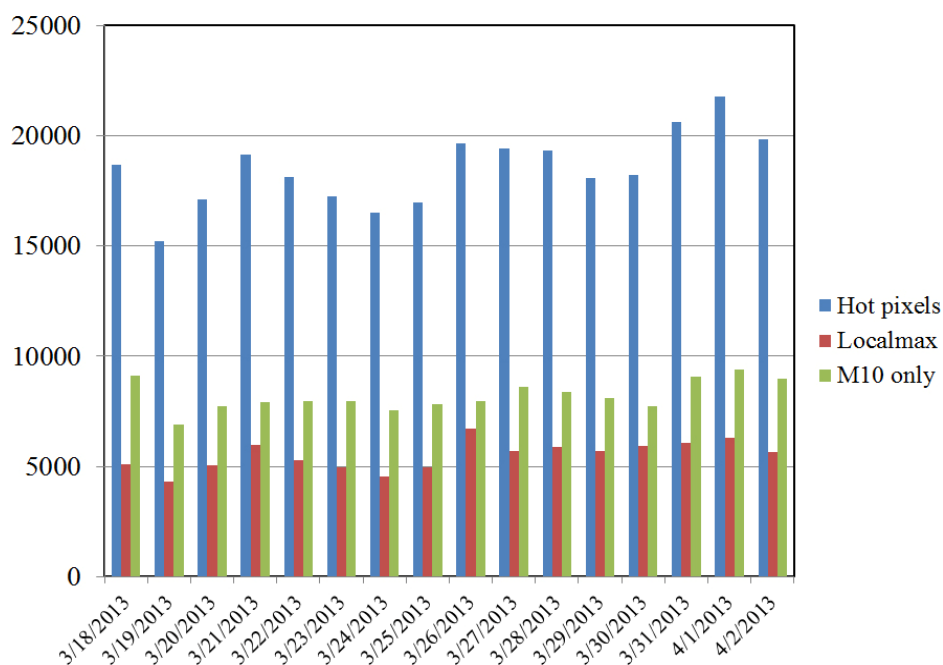
3. Results

Nightfire CSV files are generated for each M10 SDR file processed. These are then merged to form CSV files containing a full day of observations. In addition, a KMZ is generated containing data for the M10 local maxima. These output files are available at: http://www.ngdc.noaa.gov/eog/viirs/ download_viirs_fire.html. A low temporal latency version of Nightfire runs on data collected by ground stations operated by the CIMSS University of Wisconsin and Oregon State University (http://www.ngdc.noaa.gov/eog/viirs/download_cimss_fire.html), providing coverage over the continental US and portions of Canada and Mexico.

3.1. Detection Numbers

The number of confirmed (multiband detection) daily hot pixel detections ranges from 15,000 to 22,000 (Figure 6). The number of local maxima is typically 30% of the confirmed hot pixel tallies. The chart also shows tallies of pixels with only an M10 detection, where the detection of a hot pixel could not be confirmed by hot pixel detection in any other spectral band. These pixels are recorded in the CSV and marked as unconfirmed using a quality flag. The number of unconfirmed M10 detections average 44% of the confirmed detections. While many of the unconfirmed M10 detections are noise, some are genuine hot pixels with weak signals.
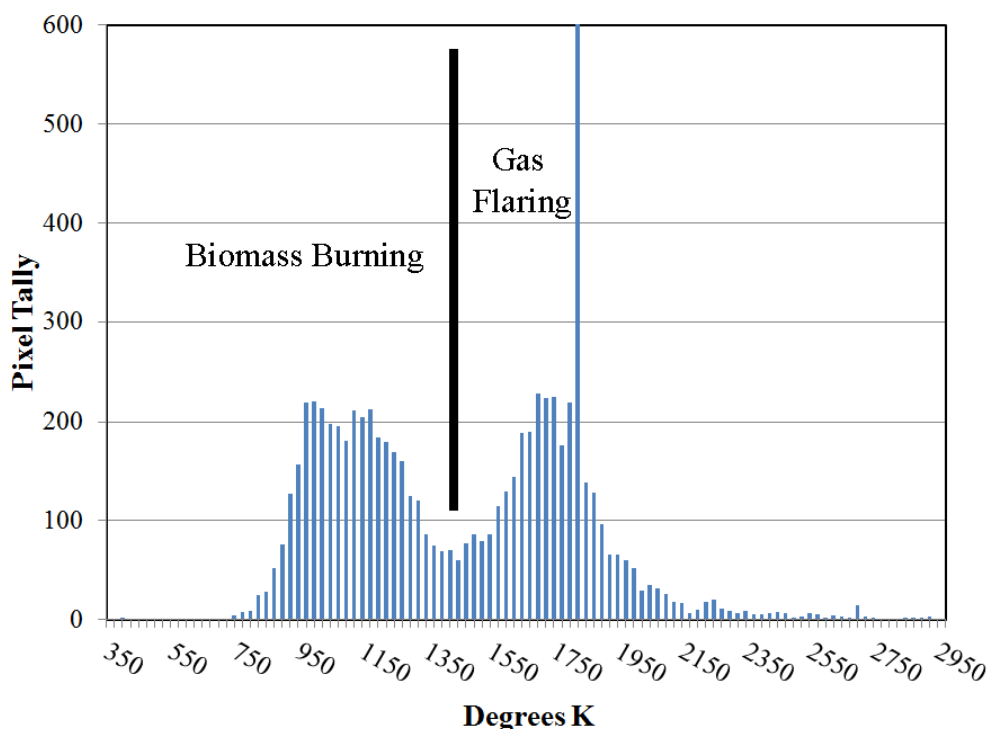
Figure 6. Tallies of Nightfire M10 hot pixels and local maxima for a sixteen day period starting 18 March 2013. The third column shows tallies of M10 detections that could not be confirmed with detection in at least one additional spectral band. These single band detections are treated as noise.

3.2. Temperature Distribution of Detections

With detections spanning from visible to MWIR, Nightfire successfully retrieves temperatures over a wide range. There is a distinctly bimodal temperature distribution to the detections (Figure 7). Biomass burning detections are primarily in the range of 600 to 1,200 K, with a median near 1,000 K. Gas flare temperatures overlap with the high end of temperatures associated with biomass burning (1,400 K) and have a median near 1,750 K. In terms of the number of local maxima detected in a day, the two predominant types of detections (biomass burning and gas flares) are on par with each other. Approximately 15% of the observations have temperatures fixed at 1,810 degrees K due to the dual-band detection style, with M10 and DNB only, as discussed in Section 2.5.

Figure 7. Histogram of temperature results from 3 July 2013. There is a spike in the histogram bin covering 1810 K due to the assumption that detections made with M10 and DNB only have peak radiant emission in the M10 spectral band.

3.3. Detection Limits

Nightfire detection limits are defined by the minimal detectable radiance of the M10 spectral band at night. Since the radiances detected in M10 are entirely from the hot sources present in the pixel footprint, the M10 minimal detectable radiance can be used to define the source area required to achieve a detection for any given temperature. Figure 8 shows a plot of a full day of Nightfire temperatures and source area estimates. Note there is a zone below the data cloud that is devoid of detections. The detection limit (red line) has been modeled with the typical nadir M10 detection limit and Planck's Law by calculating the source size required to generate a detectable M10 radiance for temperatures ranging from 500 to 2,800 K. The modeled detection limit falls along the lower surface of the data cloud, indicating that Nightfire's detection limits closely match the theoretical limits based on the M10 detection limit. The detection limit line shifts slightly upward at the edge of scan due to the gradual increase in the pixel footprint size and the increase in the M10 detection threshold, as discussed in Section 2.1. Modeled source area detection limits at nadir for a range of temperatures are shown in Table 2. The lower detection limit for Nightfire is estimated at 500 K, which is the temperature where a full pixel hot source (ESF = 1) would be required to generate a M10 detection at nadir.

On Figure 8 there is a set of seven pixels that fall below the red line, labeled as "misfits". At the low end of the temperature range (under 700 K), the radiance in M10 is low compared to M12 and M13. The Planck curve fits for misfit pixels do not pass through or even close to the M10 radiance. The results are temperature estimates that are low, pulling the pixels below the red line in Figure 8. It may be possible to address this problem with an adjustment to the Planck curve fitting procedure to add weight to the M10 radiance.

Figure 8. Plot of Nightfire temperature *vs.* source area estimates. The red line indicates the theoretical detection limit modeled based on the M10 detection limit. The green line is the hypothetical detection limit based on the published M10 minimum detectable radiance (Lmin) requirement [12].
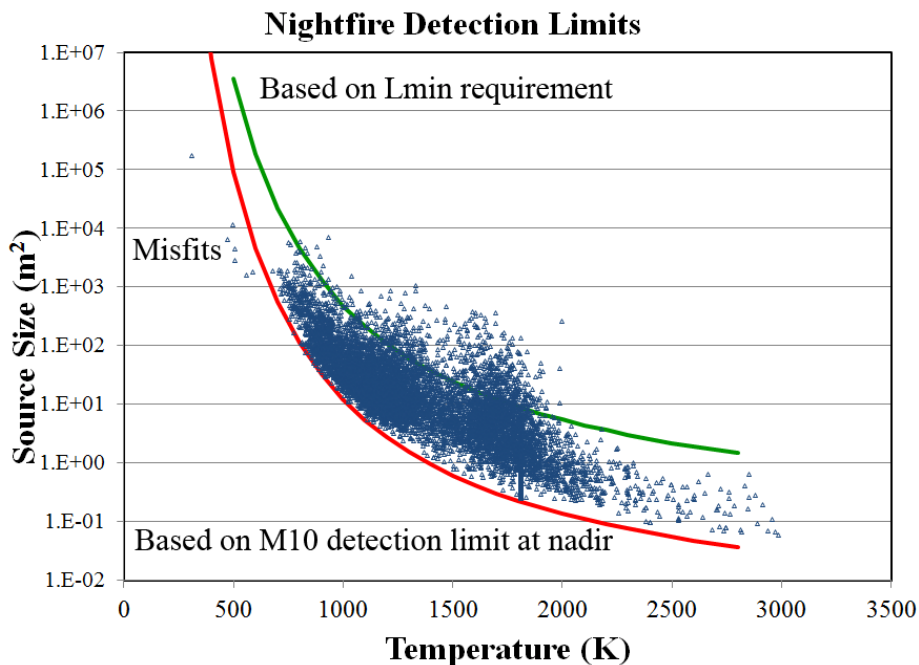

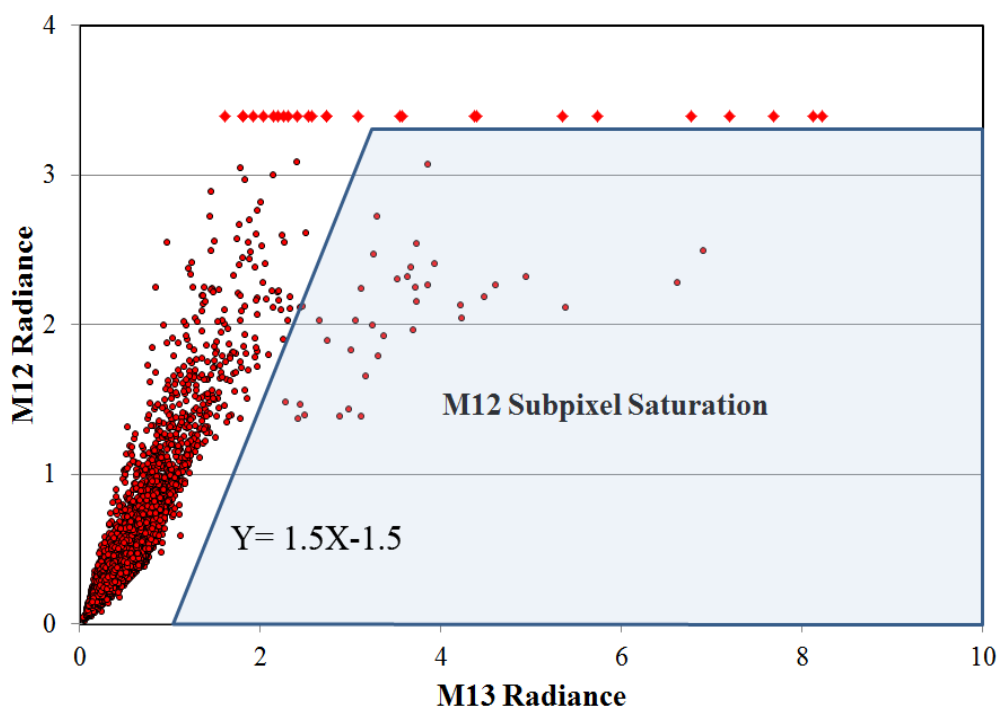**Table 2.** Nightfire Source Area Detection Limits by Temperature.

Temperature (K)	Source Area (m²)
500	104,031
600	5,298
700	631.8
800	128.2
900	37.1
1,000	13.7
1,100	6.10
1,200	3.10
1,300	1.75
1,400	1.07
1,500	0.698
1,600	0.481
1,700	0.346
1,800	0.258
1,900	0.198
2,000	0.156
2,100	0.126
2,200	0.103
2,300	0.086
2,400	0.073
2,500	0.063
2,600	0.055

<div align="center">

Table 2. *Cont.*

Temperature (K)	Source Area (m^2)
2,700	0.048
2,800	0.042
2,900	0.038
3,000	0.034

</div>

The green line in Figure 8 marks the detection limit defined based on the published detection limit (Lmin) for the M10 spectral band [12]. The published detection limit is 1.1 W/(m^2·µm·sr) (Table 1). Nightfire achieves a detection limit of 0.03 W/(m^2·µm·sr), substantially lower than the requirement Lmin.

> **Figure 9.** Plot of M13 *vs.* M12 radiances for Nightfire local maxima pixels from 4 April 2013. Across the upper tier of the chart there is a line of M12 saturated pixels pegged at the saturation radiance (3.39 W/(m^2·µm·sr)). The quality flag for these pixels is correctly set for saturation. The pixels in the shaded area exhibit the pattern expected for sub-pixel saturation and are from aggregation zones 1 and 2 (three and two pixel aggregations). The original data have no quality flag setting for sub-pixel saturation. The Nightfire algorithm identifies M12 sub-pixel saturation and records a quality flag for these pixels in the CSV.

3.4. Filtering of M12 Saturation

The only spectral band where an indication of saturation has been found for pixels containing hot sources is M12—centered at 3.8 µm. The M12 saturation radiance is 3.39 W/(m^2·µm·sr), somewhat higher than the 2.84 requirement listed in Table 1. However, there can be sub-pixel saturation in aggregation zones 1 and 2 (Figure 3). Averaging saturated and unsaturated pixels results in radiances

below the saturation radiance. Figure 9 shows M13 *vs.* M12 radiances for confirmed hot pixel detections from 4 April 2013. There is a line of pixels saturated in M12 pegged at radiances of 3.39. These were correctly indicated as saturated in the SDR quality flags. Nearly all of these fully saturated pixels are from the third aggregation zone (single pixel collections) and in this case none are from aggregation zone one (three pixel aggregation). On the right side of the chart there are pixels that are low in M12 relative to M13, falling away from the primary data cloud. All of these pixel are from aggregation zones one and two (Figure 3). These pixels did not have their SDR quality flag set for sub-pixel saturation. Examination of the full spectra for these pixels indicates that they are affected by sub-pixel saturation in M12, with anomalous dips in M12 radiance relative to M10 and M13. Currently, the pixels with M12 sub-pixel saturation are identified as falling in the shaded area on Figure 9. A quality flag is set in the CSV for pixels falling in this zone and the M12 radiance is excluded from the Planck curve fitting.

3.5. Effects of Atmospheric Correction

To examine the effects of atmospheric correction on the combustion parameters we examined plots of the temperature, source size and radiant heat with and without atmospheric correction. In the case of temperature and radiant heat, atmospheric correction results in a highly linear shift in the estimates (Figures 10 and 11). This is good news in that it indicates that non-atmospherically corrected Nightfire data could potentially be shifted to achieve the benefit of an atmospheric correction without the computational burden. The source area estimates are more heavily impacted by atmospheric correction (Figure 12). This is attributed to variability in the ESF terms derived from the Planck curve fitting.

Figure 10. Plot of local maxima temperature estimates with and without atmospheric correction from 4 April 2013. The shaded area encompasses the 99% confidence interval around the regression line.
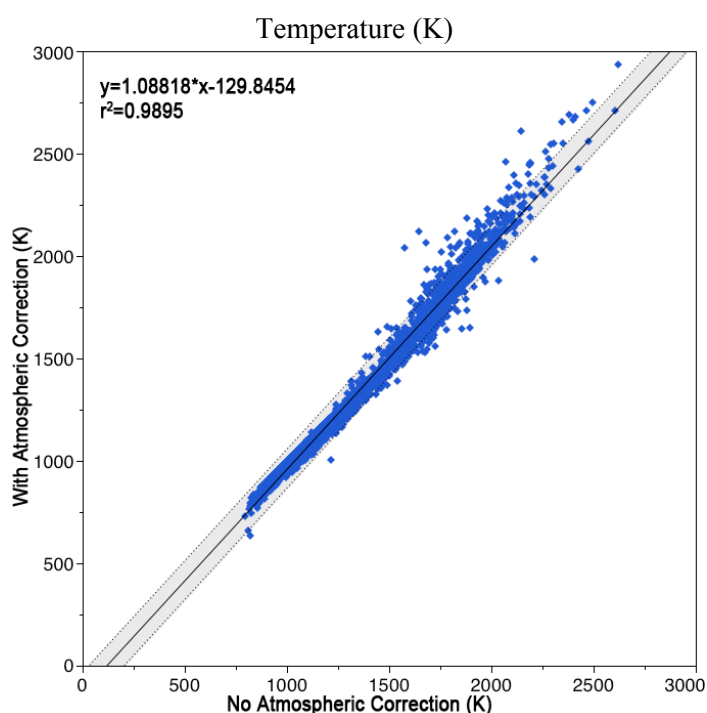

Temperature (K)

$y=1.08818*x-129.8454$
$r^2=0.9895$

Figure 11. Plot of local maxima radiant heat estimates with and without atmospheric correction from 4 April 2013. The shaded area encompasses the 99% confidence interval around the regression line.
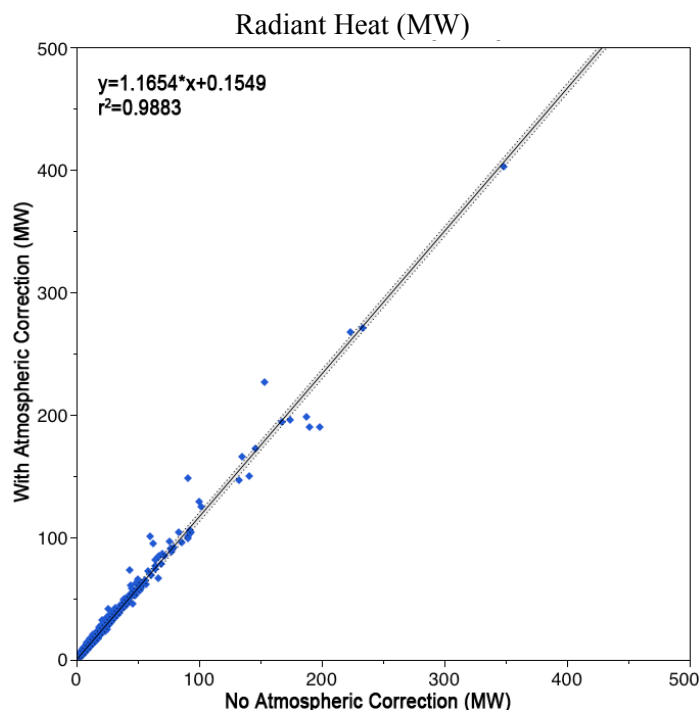

Figure 12. Plot of local maxima source area estimates with and without atmospheric correction from 4 April 2013. The shaded area encompasses the 99% confidence interval around the regression line.
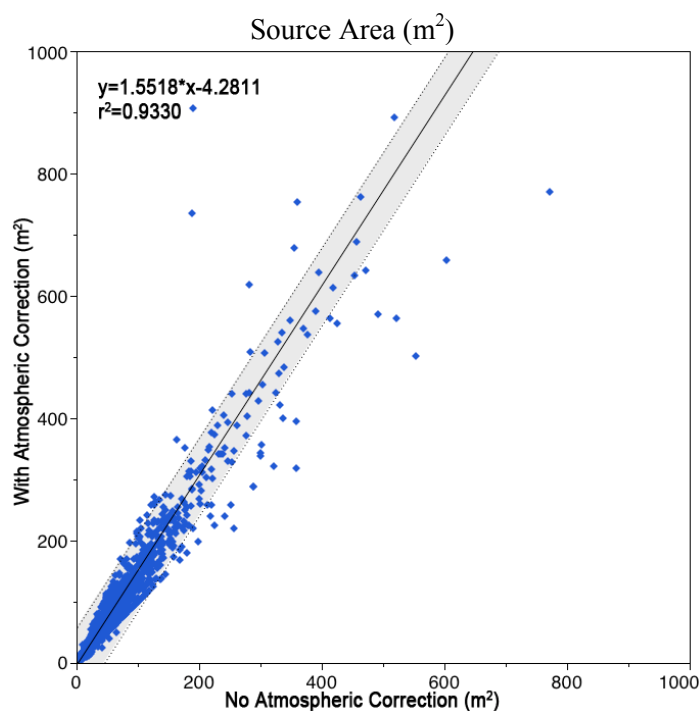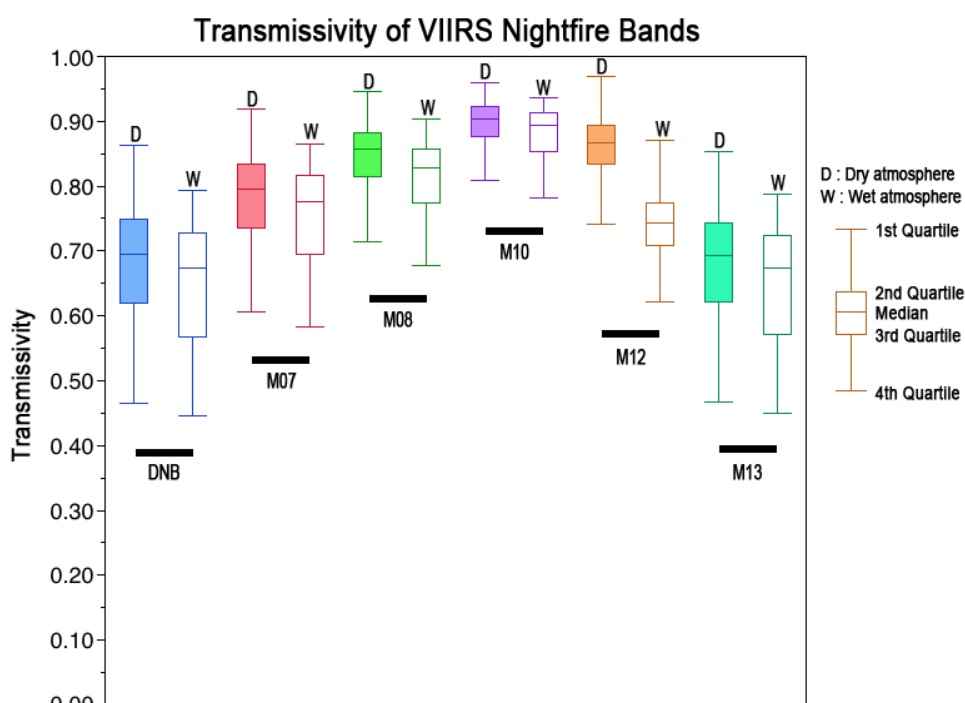

Another test was performed to compare the transmissivity of the six spectral bands used in Nightfire for two distinctly different atmospheres: wet *vs.* dry. The MODTRAN model was run for Nightfire

detections in the Iraq region (dry atmosphere) and Nigeria region (wet atmosphere). The transmissivities were analyzed to identify the median and quartiles. For each spectral band the transmissivities through the wet atmosphere are lower (Figure 13). The band with the highest transmissivity is M10, with a median near 90% transmissivity for both the wet and dry atmosphere. In addition, the quartile range of transmissivities is narrowest for the M10 spectral band. In contrast, the DN Band M13 have median transmissivities near 70% and wide dispersion in transmissivities, as indicated by the quartiles. Inclusion of the M10 spectral band in the Planck curve fitting may explain the relatively minor atmospheric effects on temperature and radiant heat estimates shown in Figures 10 and 11.

Figure 13. Plot of median and four quartiles for the MODTRAN derived transmissivity of the six spectral bands used in Nightfire for a wet and a dry atmosphere. Processed from Nightfire detections for 2 June 2013.
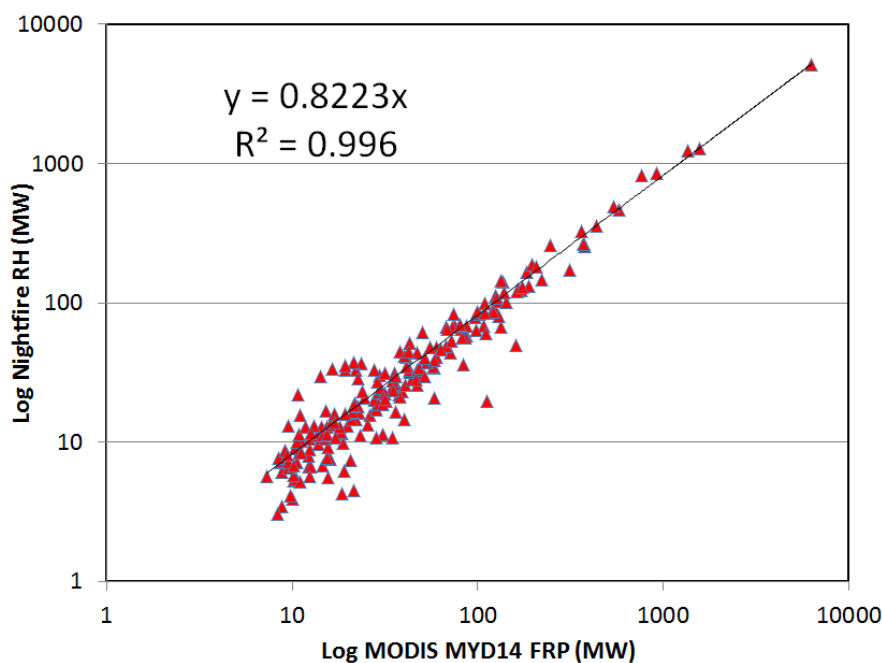

4. Validation

Nightfire is a new data product that will take some time for full validation. However, the authors are able to report a limited set of validation results at this time. This includes comparisons with MODIS active fire product, the operational VIIRS active fire product, an accuracy assessment for the identification of gas flares, temperature stability of a gas flare, and temperature of a high temperature xenon-arc sky beam.

4.1. Intercomparison with MODIS Fire Radiant Power

Nightfire radiant heat (RH) was compared to MODIS Aqua Fire Radiative Power (FRP) for 471 individual clusters of fire detections observed during a major outburst of burning in Sumatra which occurred on 19 June 2013. The units for RH and FRP are the same (MW). The two sensors collected data over Sumatra within six minutes of each other. The analysis was confined to land since offshore gas flare detections are excluded from the MODIS product. FRP and RH gridded images were produced

at 15 arc second resolution. The MODIS active fire product cloud masking procedure was applied to the Nightfire data to further narrow differences between the two datasets. An automatic clustering algorithm identified overlapping Nightfire and MODIS cloud-free pixel clusters and summed the MW signal. Figure 14 indicates that the MODIS FRP and Nightfire RH are highly correlated.

Figure 14. Plot Nightfire Radiant heat (MW) *vs.* MODIS Fire Radiative Power (MW) from 471 fire clusters observed within six minutes of each other on 19 June 2013.
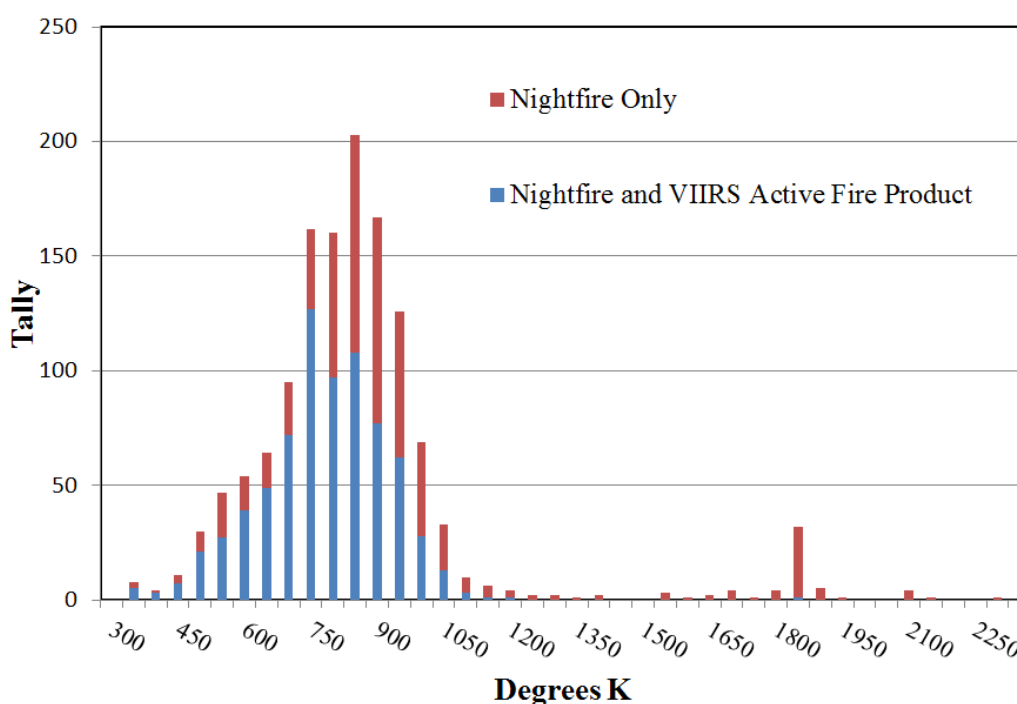

4.2. Intercomparison of VIIRS Active Fire Product and Nightfire

An intercomparison of Nightfire with the VIIRS active fire product was conducted for the 19 June 2013 Sumatra fires described in Section 4.1. Since the operational VIIRS active fire product only provides a list of pixels containing fires, the intercomparison is limited to analyzing the number of detections they have in common *vs.* the number of detections that are unique to one of the two products. As with the MODIS intercomparison, the VIIRS active fire cloud masking procedure was followed to ensure the comparsion covered the same areas. Water areas were also masked, since the VIIRS active fire product only reports hot pixels on land surfaces. Neither product was filtered to remove bow-tie duplicates. The results are summarized in Table 3. Fifty-three percent of the total number of fire detections were observed by both sensors. The VIIRS operational product detected 81 fire pixels (6%) that were not reported by Nightfire. Nightfire had 578 detections (41% of the total) that were missing in the VIIRS active fire product. Because there are gas flares present on Sumatra, a check was made to see if the large number of Nightfire unique detections could be due to under-detection of high temperature gas flares by the VIIRS active fire product. In actuality, the Nightfire unique detections are distributed across a wide range of temperatures (Figure 15), with 83% in the primary temperature range of biomass burning (550 to 1,050 K). The authors attribute the larger number of detections in the Nightfire data to the lack of scene background effects on the M10 hot pixel detection thresholding.

Table 3. Intercomparison of VIIRS Active Fire *vs.* Nightfire Pixel Detection Numbers in Sumatra from 19 June 2013.

Type	Pixel Tally	Percent of Total
Nightfire & VIIRS Active Fire Product	741	53%
Nightfire Unique	578	41%
VIIRS Active Fire Product Unique	81	6%
TOTAL	1400	100%

Figure 15. Histogram of temperatures for the pixels detected by the VIIRS active fire product and Nightfire (blue) *vs.* Nightfire only (red). Data are from the 19 June 2013 Sumatra intercomparison.

4.3. Temperature Stability of a Gas Flare

The primary combustible gas feeding the typical gas flare is methane. The temperature of a flare is largely determined by the composition of the gases and combustion efficiency. It is known that the quantity and composition of gases dissolved in petroleum in an oil field change slowly over the production lifetime. Based on this, it is reasonable to expect that over a time span such as a month, the temperature of a gas flare would be largely stable. Figure 16 shows the temperature of a gas flare in Iraq, with thirty observations in the month of January 2013. The temperature is stable, with an average of 1720 K and a standard deviation of 61 K.

4.4. Accuracy of Gas Flare Identifications

Gas flares should be identifiable based on their high temperature and temporal persistence. To test the ability of Nightfire data to correctly identify gas flares, a validation was conducted using a cloud-free composite of Nightfire data from January 2013. The detections were sorted to yield a set that had average temperatures greater than 1,600 K and detection in at least 20% of the cloud-free

observations. This subset was converted into a KMZ for display using Google Earth. For each point, an analyst reviewed the base image present in Google Earth to see if a gas flare or gas flare infrastructure features could be identified (e.g., Figure 17). If no gas flare could be located, the analyst noted the type of base image data and year of the base image data. The points for which no gas flare could be found in Google Earth were filtered to remove cases where the base imagery had coarse spatial resolution (e.g., Landsat) or the image data were older than 2012. The filtered set was then used to discount the percent accuracy of the gas flare identifications. The results are presented in Table 4. The overall accuracy was 99%, indicating that temperature and temporal persistence can be used to filter Nightfire detections for the identification of gas flares.

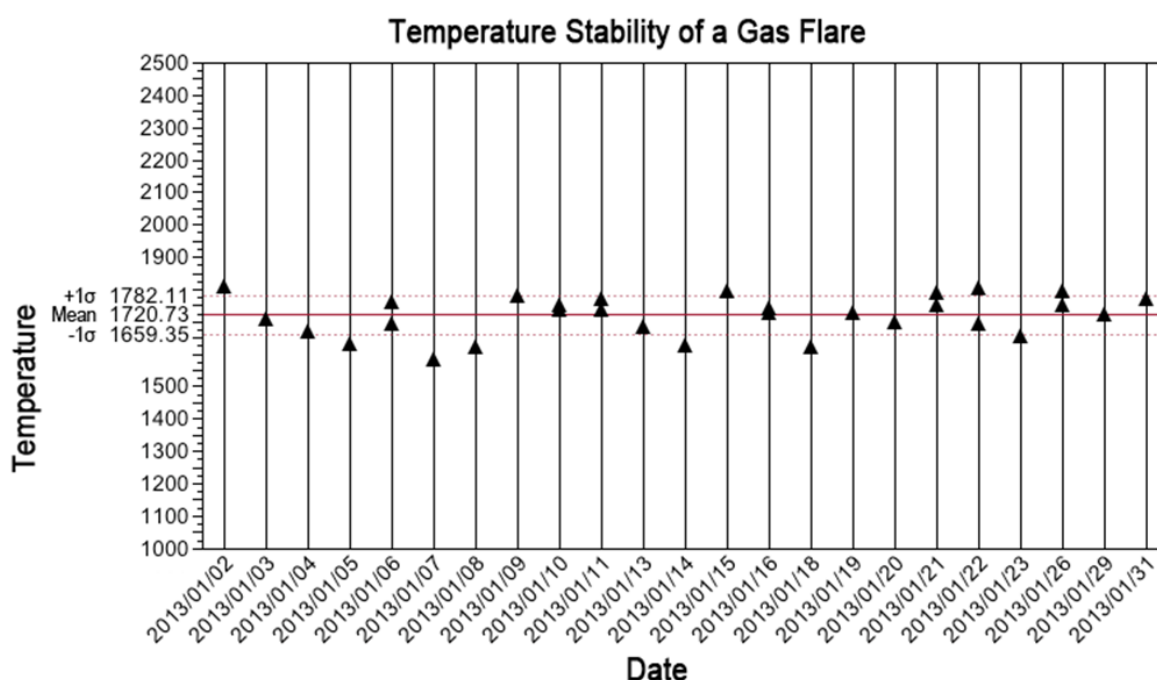**Figure 16.** Temperature stability of a gas flare in Basra, Iraq during the month of January 2013.

Table 4. Percent accuracy of Nightfire gas flare identifications from January 2013.

Country	Flares Identified	Unknown	Percent Accuracy
Algeria	118	0	100%
Bahrain	6	0	100%
Egypt	78	1	99.73%
Iran	142	0	100%
Iraq	91	0	100%
Kuwait	48	0	100%
Libya	80	0	100%
Oman	55	0	100%
Qatar	18	1	94.74%
Saudi Arabia	89	5	94.68%
Syria	26	0	100%
UA Emirates	25	1	96.15%
Yemen	25	0	100%
Total	**807**	**8**	**99.01%**

Figure 17. Example of a gas flare in Google Earth base imagery from Digital Globe. The site has a fireball and pipeline structures. In other cases the flare is not active and the flare stack or pipeline is visible.

Figure 18. The Luxor sky beam.

4.5. Temperature of the Luxor Sky Beam

The Luxor sky beam (Figure 18) in Las Vegas, Nevada is widely recognized as the brightest light shining into the sky. The sky beam is generated with a set of 39 closely spaced 7,000 Watt xenon arc lamps with reflective casings. The lamps are rated at a 6,000 K color temperature [20]. The lights are focused into a single beam, aimed straight up into the sky. On 7 July 2013, VIIRS data were collected with the sky beam at nadir. The radiances are high in DNB and M7, and trailing off to lower radiances in M8 and M10. The sky beam was not detected in M12 or M13. The Planck curve fit came out to 6,000 K, matching the temperature quoted for 7,000 W xenon arc lamps [20]. The source size estimate is 0.2 m^2, which is interpreted as an estimate of the aggregated area of the 39 xenon plasmas generating the sky beam. The Luxor sky beam radiances and Planck curve fit are in the upper left corner of Figure 19, marked as 6,000 K.

Figure 19. Nightfire Planck curve fits spanning 600 to 6,000 degrees K. The 6,000 K curve is from the Luxor sky beam.
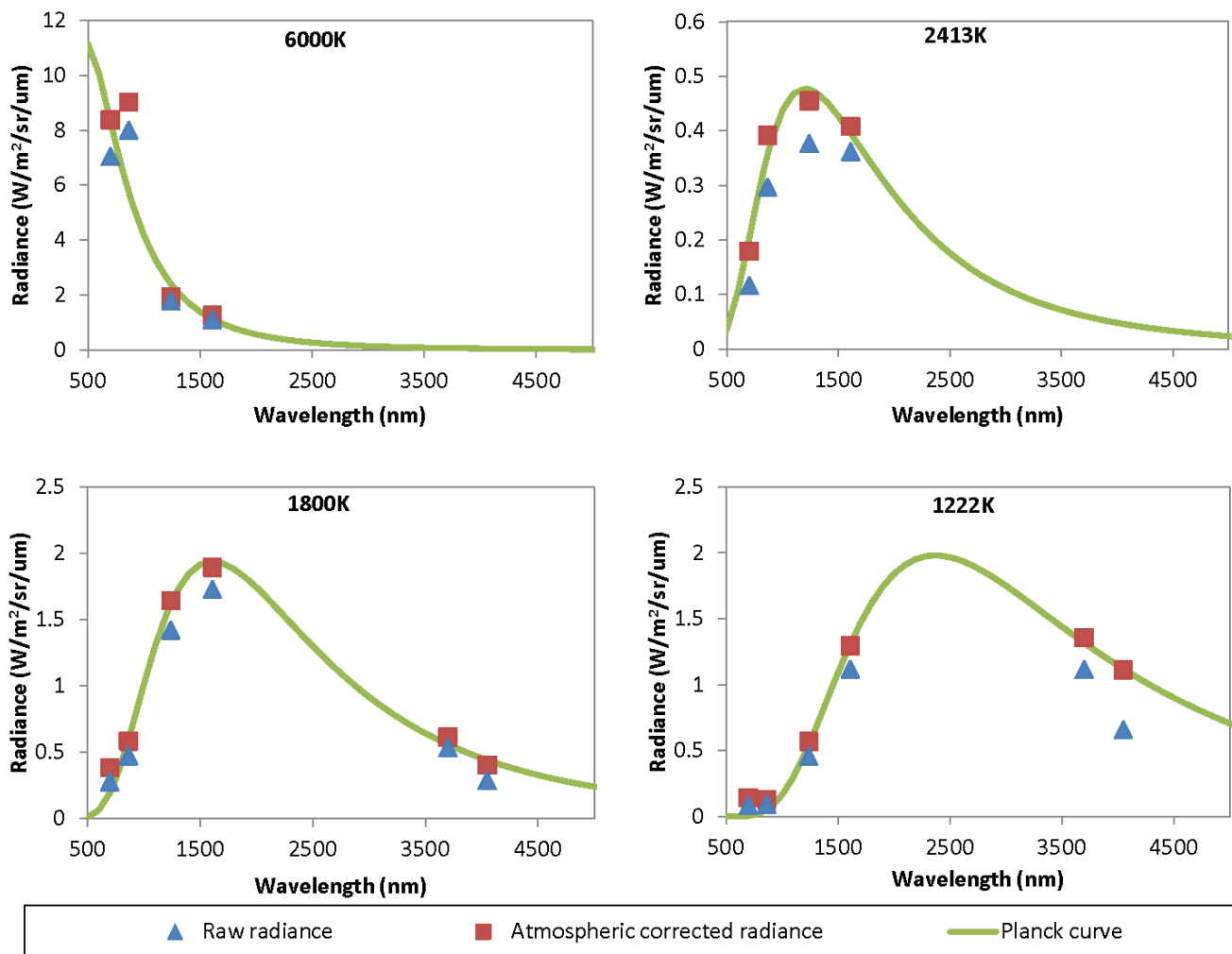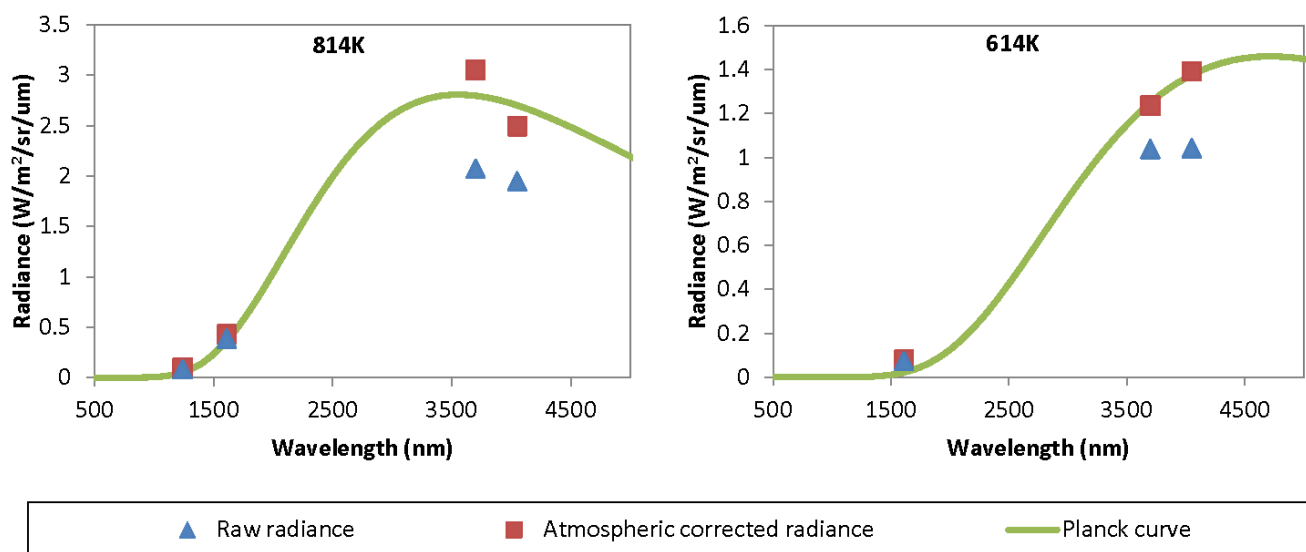
Figure 19. *Cont.*

5. Conclusions

NGDC has developed a system called Nightfire, which detects and characterizes sub-pixel combustion sources worldwide using nighttime data collected by the NASA-NOAA Suomi NPP Visible Infrared Imaging Radiometer Suite (VIIRS). Nightfire takes advantage of data collected at night by NIR and SWIR spectral bands designed for daytime imaging. With sunlight eliminated these bands record background noise, punctuated by high radiant emissions in pixels containing combustion sources. With multispectral detections spanning the visible to the MWIR it is possible to fully model the Planck curves of sub-pixel heat sources, enabling the estimation of temperature, source size, and radiant heat. Similar instruments, such as MODIS and AVHRR shut down the collection of data from daytime imaging bands at night, presumably to reduce data downlink and processing effort.

Initial detection of pixels containing combustion sources is made in the VIIRS M10 band, centered in the SWIR at 1.6 μm. The radiances from five additional spectral bands (DNB, M7, M8, M12, and M13) are examined to determine if they are also hot. Radiances from M7–10 are attributed to the hot source since the noise background values are extremely low and by design average to zero in aggregate. Background subtraction is required to calculate combustion source radiances in M12 and M13. The hot source radiances are used to model the Planck curve using temperature and emission scaling factor (ESF) as fitting variables. The sources appear as gray-bodies due to the fact that they are substantially smaller than the pixel footprints. Nightfire reports the temperature (degrees K), source size (m^2), and radiant heat (MW) of sub-pixel hot sources. Gas flares can generally be distinguished from biomass burning, active volcanoes, and industrial sites, such as steel mills, based on their high temperature. Nightfire data can be accessed at http://www.ngdc.noaa.gov/eog/data/viirs_fire/viirs_html/download_viirs_fire.html. NGDC is working on a calibration for estimating flared gas volumes from Nightfire data.

Nightfire is similar to the Dozier method [1] in that the procedure is conducted with nighttime satellite data and the objective is to calculate the temperature and source size for sub-pixel hot objects. The classic Dozier method uses a 4 μm MWIR band and an 11 μm LWIR band, spectral bands

designed for the observation of clouds and the earth surface. A major problem with the classic Dozier method is that it is only applicable to pixels where the hot source is detected in both the MWIR and LWIR. Because the LWIR is on the trailing edge of hot source Planck curves, very few pixels with hot source signal in the MWIR also have signal in the LWIR. In addition, methods used to estimate background temperature and atmospheric effects in MWIR and LWIR result in error effects in temperature and source size estimates.

Nightfire mitigates MWIR scene background errors with hot source radiances measured against sensor noise backgrounds in three spectral bands: M7, M8, and M10. With zero radiance from the scene background in these bands when collected at night, the full measured radiance can be attributed to the infrared emitter with no ambiguity. Atmospheric effects on detection and estimation of temperature and source size are reduced through reliance on the 1.6 μm (M10) spectral band which is in a very clear atmospheric window (Figure 13). By expanding the number of spectral bands and widening the wavelength range (from visible to MWIR), Nightfire is able to retrieve temperatures spanning from 600 to 6,000 K (Figure 18).

Another major difference between the Dozier method and Nightfire is the vast expansion in the number of pixels for which temperature and source size retrievals are possible. Dozier could only find a handful of pixels with hot source signal in both the 3.7 and 11 μm channels on a typical night. It is rare to get hot source detection in the 11 μm channel. In contrast, Nightfire is producing temperature and source area retrievals for fifteen to twenty thousand VIIRS pixels every night.

Five types of validation analyses have been performed on Nightfire data. To compare MODIS FRP (MW) with Nightfire radiant heat (MW), a study was done for a large set of fires observed in Sumatra during June of 2013. The VIIRS and MODIS data were collected within six minutes of each other. MODIS FRP and VIIRS radiant heat were found to be highly correlated with each other. Comparison of the VIIRS active fire product with Nightfire in the Sumatra data set revealed that Nightfire detects substantially more fire pixels, probably due to Nightfire's ability to detect hot pixels in M10 with no scene background effects. The temperature stability of an individual gas flare was demonstrated using data from a full month. Finally, the 6,000 K temperature of the Las Vegas, Nevada Luxor sky beam was confirmed with a 6,000 K Planck curve fit with Nightfire data.

There are some problems with the current version of Nightfire that the authors continue to work on. The Planck curve fitting results in unrealistic fits for certain pixels in the 500 to 700 K range. We attribute this to errors in the M12 and M13 background removal. The authors are exploring the possibility of adding an independent M12 and M13 hot pixel detection and analysis system that would be coupled to the short-wave Nightfire detection system. The other major weakness of Nightfire is the large number of pixels for which a M10 detection goes unconfirmed by any other spectral band or only with the DNB. The best solution for this would be to have M11 (2.2 μm) data collected at night by VIIRS. The M11 Lmin requirement is ten times lower than the M10 band. The authors believe that having M11 data at night would enable full Planck curve fitting for thousands of additional pixels every day and assist in noise filtering.

It could be argued that observations of combustion sources after midnight are of limited value. The majority of fires start during daytime hours when ambient temperatures and human activity levels are higher. Thus, the after midnight overpass of the SNPP likely under represents the extent of biomass burning. There are no known diurnal patterns known for gas flaring, which is the other type of

phenomenon widely detected in Nightfire data. The advantage of Nightfire over other global fire observation data sources is the ability to consistently model Planck curves from sub-pixel heat sources over a wide span of temperatures. To our knowledge, it is the only satellite fire detection system which estimates temperature and source size for biomass burning, gas flares, and volcanoes worldwide on a daily basis.

Acknowledgments

Conflict of Interest

The authors declare no conflict of interest.

References

1. Dozier, J. A method for satellite identification of surface temperature fields of sub-pixel resolution. *Remote Sens. Environ.* **1981**, *11*, 221–229.
2. Giglio, L.; Kendall, J.D. Application of the Dozier retrieval to wildfire characterization—A sensitivity analysis. *Remote Sens. Environ.* **2001**, *77*, 34–49.
3. Peterson, D.; Wang, J. A sub-pixel-based calculation of fire radiative power from MODIS observations: 2. Sensitivity analysis and potential fire weather application. *Remote Sens. Environ.* **2013**, *129*, 231–249.
4. Peterson, D.; Wang, J.; Ichoku, C.; Hyer, E.; Ambrosia, V. A sub-pixel-based calculation of fire radiative power from MODIS observations: 1. Algorithm development and initial assessment. *Remote Sens. Environ.* **2013**, *129*, 262–279.
5. Zhukov, B.; Lorenz, E.; Oertel, D.; Wooster, M.; Roberts, G. Spaceborne detection and characterization of fires during the bi-spectral infrared detection (BIRD) experimental small satellite mission (2001–2004). *Remote Sens.Environ.* **2006**, *100*, 29–51.
6. Justice, C.; Giglio, L.; Boschetti, L.; Roy, D.; Csiszar, I.; Morisette, J.; Kaufman, Y. *MODIS Fire Products: Algorithm Technical Background Document*; 2.3.1 Version; University of Maryland: College Park, MD, USA, 2006.
7. Giglio, L.; Csiszar, I.; Justice, C.O. Global distribution and seasonality of active fires as observed with the Terra and Aqua Moderate Resolution Imaging Spectroradiometer (MODIS) sensors. *J. Geophys. Res.* **2006**, *111*, G02016.
8. Kaufman, Y.J.; Justice, C.O.; Flynn, L.P.; Kendall, J.D.; Prins, E.M.; Giglio, L.; Ward, D.E.; Menzel, W.P.; Setzer, A.W. Potential global fire monitoring from EOS-MODIS. *J. Geophys. Res.* **1998**, *103*, 32215–32238.
9. Elvidge, C.D.; Ziskin, D.; Baugh, K.E.; Tuttle, B.T.; Ghosh, T.; Pack, D.W.; Erwin, E.H.; Zhizhin, M. A fifteen year record of global natural gas flaring derived from satellite data. *Energies* **2009**, *2*, 595–622.

10. Casadio, S.; Arino, O. ATSR-WFA New Algorithms for Hot Spot Detection. In Proceedings of the 2nd MERIS/(A)ATSR User Workshop, European Space Agency SP-666, Frascati, Italy, 22–26 November 2008.

11. Casadio, S.; Arino, O.; Serpe, D. Gas flaring monitoring from space using the ATSR instrument series. *Remote Sens. Environ.* **2012**, *116*, 239–249.

12. Cao, C.; DeLuccia, F.; Xiong, X.; Wolfe, R.; Weng, F. Early on-orbit performance of the Visible Infrared Imaging Radiometer Suite (VIIRS) onboard the Suomi National Polar-orbiting Partnership (S-NPP) satellite. *IEEE Trans. Geosci. Remote Sens.* **2013**, doi:10.1109/TGRS.2013.2247768.

13. Berk, A.; Anderson, G.P.; Acharya, P.K.; Shettle, E.P. *MODTRAN5.2.0.0 User's Manual*; Air Spectral Sciences, Inc.: Burlington, MA, USA and Force Research Laboratory: Hanscom, MA, USA, 2008.

14. Baker, N. *Joint Polar Satellite System (JPSS) Operational Algorithm Description (OAD) Document for Cross-track Infrared and Advanced Technology Microwave Sounder Suite (CrIMSS) Environmental Data Record (EDR) Software*; C Revision; NASA-GSFC: Greenbelt, MD, USA, 2013.

15. Zhizhin, M.; Elvidge, C.D.; Hsu, F-C.; Baugh, K.E. Using the short-wave infrared for nocturnal detection of combustion sources in VIIRS data. *Proc. Asia-Pacific Adv. Netw.* **2013**, *35*, 49–61.

16. Lagarias, J.C.; Reeds, J.A.; Wright,M.H.; Wright, P.E. Convergence properties of the Nelder-Mead simplex method in low dimensions. *Siam J. Optim.* **1998**, *9*, 112–147.

17. Ichoku, C.; Kaufman, Y.J. A method to derive smoke emission rates from MODIS fire radiative energy measurements. *IEEE Trans. Geosci. Remote Sens.* **2005**, *43*, 2636–2649.

18. Bussman, W.; Hong, J. Flare Radiation. In *Industrial Combustion Testing*; Charles, E.B., Jr., Ed.; CRC Press: Boca Raton, NY, USA, 2010; pp. 595–611.

19. Baker, N. *Joint Polar Satellite System (JPSS) VIIRS Cloud Mask (VCM) Algorithm Theoretical Basis Document (ATBD)*, Revision B; NASA-GSFC: Greenbelt, MD, USA, 2008.

20. Xenon Short Arc Lamps. Available online: http://www.sqpuv.com/PDFs/TechnicalSpecificationGuide.pdf (accessed on 9 July 2013).